Published in final edited form as:

J Chem Theory Comput. 2023 July 25; 19(14): 4414–4426. doi:10.1021/acs.jctc.3c00028.

Discovering reaction pathways, slow variables, and committor probabilities with machine learning

Haochuan Chen[†], **Benoît Roux**[‡], **Christophe Chipot**[†,¶,‡]

[†]Laboratoire International Associé Centre National de la Recherche Scientifique et University of Illinois at Urbana-Champaign, Unité Mixte de Recherche n°7019, Université de Lorraine, B.P. 70239, 54506 Vandœuvre-lès-Nancy cedex, France

[‡]Department of Biochemistry and Molecular Biology, University of Chicago, Chicago, USA

[¶]NIH Center for Macromolecular Modeling and Bioinformatics, Beckman Institute for Advanced Science and Technology, and Department of Physics, University of Illinois at Urbana-Champaign, Urbana, Illinois 61801, USA

Abstract

A significant challenge faced by atomistic simulations is the difficulty, and often impossibility, to sample the transitions between metastable states of the free-energy landscape associated to slow molecular processes. Importance-sampling schemes represent an appealing option to accelerate the underlying dynamics by smoothing out the relevant free-energy barriers, but require the definition of a suitable reaction-coordinate (RC) models expressed in terms of compact low-dimensional sets of collective variables (CVs). While most computational studies of slow molecular processes have traditionally relied on educated guesses based on human intuition to reduce the dimensionality of the problem at hand, a variety of machine-learning (ML) algorithms have recently emerged as powerful alternatives to discover a meaningful CV capable of capturing the dynamics of the slowest degrees of freedom. Considering a simple paradigmatic situation in which the long-time dynamics is dominated by the transition between two known metastable states, we compare two variational data-driven ML methods based on Siamese neural networks aimed at discovering a meaningful RC model—the slowest decor-relating CV of the molecular process, and the committor probability to first reach one of the two metastable states. One method is the state-free reversible variational approach for Markov processes networks (VAMPnets), or SRVs—the other, inspired by the transition path theory framework, is the variational committor-based neural networks, or VCNs. The relationship and the ability of these methodologies to discover the relevant descriptors of the slow molecular process of interest is illustrated with a series of simple model systems. We also show that both strategies are amenable to importance-sampling

chipot@illinois.edu .

Supporting Information Available

Demonstration of the relationship between left- and right-eigenfunctions, quantitative analyses of the similarity of the learned committor functions and the learned CVs, comparison of the learned committor functions from short unbiased and biased trajectories, transition rates, learned committor functions from PCV biased trajectories based on the physical and the unphysical pathways, necessity of an SNN architecture, and reference free-energy landscape of the isomerization of NANMA are provided in the Supporting Information.

schemes through an appropriate reweighting algorithm that approximates the kinetic properties of the transition.

Graphical Abstract

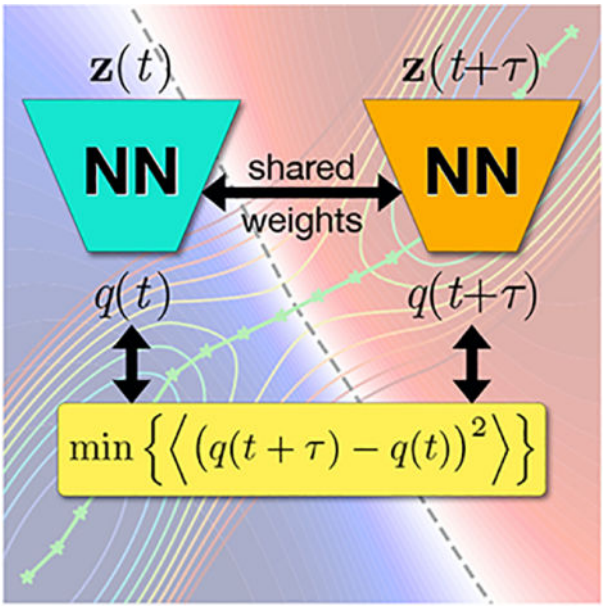

1 Introduction

A central problem in computational biophysics is the characterization of the slow conformational dynamics of complex molecular processes. Conceptually, long-time-scale kinetic processes are expected to evolve according to some rare transitions between metastable states of the free-energy landscape. In a general situation, one might not have any information about the metastable states involved, i.e., how many there are and what they are. Discovering all the relevant metastable states and characterizing all the slow molecular processes between them from molecular dynamics (MD) simulations remains a daunting challenge, not only from a computational perspective, but also from a theoretical one.

This challenge is deeply rooted in the timescales amenable to MD simulations routinely performed on common, unspecialized computer architectures, which are orders of magnitude smaller than those spanned by slow molecular processes, like the broad conformational transitions undergone by some biological object of interest.[1] A molecular process assumed to be ergodic will appear somewhat non-ergodic owing to the slow diffusion and incomplete sampling imposed by high free-energy barriers demarcating distinct volumes of configurational space. These energetic barriers are crossed so rarely that the molecular process is trapped kinetically in metastable states of the free-energy landscape, rendering the estimation of statistical averages physically meaningless. A practical solution to remedy the symptoms of such quasi-non-ergodicity scenarios consists in turning to importance-sampling strategies[2,3] aimed at overcoming free-energy barriers otherwise insuperable over the common lengths of MD simulations.

Many of these enhanced sampling strategies lean on a low-dimensional, coarse-grained model of reaction coordinate (RC) of the molecular process through the introduction of collective variables (CVs) defined as functions of the Cartesian variables.[4,5] By applying an external bias along such CVs, one aims to flatten the free-energy landscape and increase the dynamical exploration, yielding a more uniform sampling between the relevant volumes of configurational space. Although free energy is a state function, and its determination is path-invariant, the efficiency of the biasing scheme is intimately related to the choice of the CVs, which are expected to provide a reasonable representation of the free-energy landscape, allowing its metastable states to be adequately differentiated, while rendering an acceptable picture of the dynamics of the molecular process of interest. For a gamut of simple molecular processes, coarse-graining has often relied on human intuition and educated guesses, with the assumption of timescale separation, that is, the CV along which preferential sampling[6] is performed is essentially decoupled from other slow degrees of freedom. Under most circumstances, however, guessing the CVs that would depict a faithful representation of the underlying dynamics is nearly impossible, in particular when the molecular process at hand consists of entangled movements,[7] thereby providing the impetus for alternate coarse-graining strategies.

In the past twenty years, a variety of approaches aimed at discovering CVs have emerged,[8–16] leaning on a broad range of dimensionality-reduction schemes, among which unsupervised machine-learning (ML) techniques have recently elicited much interest.[17–23] The ever-growing popularity of this methodology can be understood in the promise to represent the CVs as the latent space of dimensionality-reduction schemes from the configurational space sampled by MD simulations. Towards this end, a number of avenues have been explored, training neural-network (NN) architectures with large data sets produced by equilibrium, unbiased and biased simulations. Strategies leaning on autoencoders[24] (AEs) have proven particularly powerful to construct from either generalized or Cartesian coordinates a low-dimensional latent space that maximizes the explained variance. Yet, classical AEs, agnostic to temporality, have limitations in their own right, and in many instances, are unable to discriminate between high-variance and slowly-decorrelating variables.[25,26] The transitions at hand are often burdened by slow degrees of freedom (DOFs). One may use these slow DOFs to construct the so-called “slow variables” as CVs. From this viewpoint, a variety of schemes have been put forth to account for time explicitly in the training of the NN, but mere incorporation of a temporal information in the learning process is in general insufficient to preclude encoding of mixtures of high-variance and slow modes. State-free variational approach for Markov processes networks[27] (VAMPnets), or SRVs,[28] which extracts the eigenfunctions from the spectral decomposition of the transfer operator, represent a very promising option for iterative learning of CVs based on enhanced-sampling simulations, given a suitable reweighting strategy to preserve the dynamics of the molecular process at hand.[26,29]

Ultimately, discovering all the relevant metastable states of a complex multi-dimensional system without any prior knowledge can be exceedingly challenging. For the sake of clarity, it is instructive to consider a simple paradigmatic situation, in which the long-time dynamics is dominated by the transition between two known metastable states, referred

to as A and B. In this context, the transitions between the two metastable states can be characterized using the framework of transition path theory (TPT).[30] An important ingredient of TPT is the committor probability, q, that a trajectory initiated at some random configuration will ultimately reach state B before crossing state A.[30–38] A variety of approaches have been devised to model the RC underlying complex molecular processes by means of the committor probability. These approaches share the common denominator of shooting trajectories, either assuming a stochastic dynamic model, like a Markov state model,[39] or turning to milestoning[40] with a nonequilibrium steady-state distribution from weighted-ensemble simulations,[41] using extended AEs with extra labeling for the metastable states,[42] solving the backward Kolmogorov equation,[43] or, alternatively, determining the committor probability through a variational form of its time-correlation function[38,44,45] by a nonparametric method.[46,47] Such a variational form enables us to optimize any chosen function to approximate the actual committor probability.

In the present contribution, we compare the performance of two variational data-driven ML strategies based on Siamese NN (SNN) aimed at discovering the relevant descriptors of the slow molecular process of interest in a complex system. The first strategy is the state-free variational spectral decomposition of Markov processes networks[8,27,48] (VAMPnets) or SRVs.[28] The second strategy, coined as variational committor-based neural networks (VCNs), relies on a variational formulation of the committor probability within the framework of TPT.[30,38,44] In both approaches, we optimize the NN-modeled functions based on specific time-correlation functions with a reweighting approach, using trajectories from biased MD simulations as the training data. The close correspondence between the two approaches is illustrated for a series of model systems. We also show that both strategies are amenable to importance-sampling schemes through an appropriate reweighting algorithm that approximates the kinetic properties of the transition.

2 Theory and Methods

2.1 Effective dynamical propagator, spectral analysis, and committor

The configuration of a molecular system of interest is completly determined by the Cartesian coordinates $\mathbf{x} \equiv \{x_1, x_2, \ldots, x_N\}$. To reduce the complexity of the problem, one typically seeks to represent the molecular system within the subspace of reduced dimension spanned by a sub-set of CVs, $\mathbf{z}(\mathbf{x}) = \{z_1(\mathbf{x}), \ldots, z_n(\mathbf{x})\}$ where $n \ll N$, i.e., a vector-valued function that maps every Cartesian configuration x of the system on a set of values $\mathbf{z}$. Accordingly, the equilibrium distribution within the subspace of the CVs is formally written as,

$$\rho_{\mathrm{eq}}(\mathbf{z}^*) = \frac{\int d\mathbf{x}\, \delta(\mathbf{z}(\mathbf{x}) - \mathbf{z}^*) e^{-U(\mathbf{x})/k_{\mathrm{B}}T}}{\int d\mathbf{x}\; e^{-U(\mathbf{x})/k_{\mathrm{B}}T}} \tag{1}$$

where $U(\mathbf{x})$ is the microscopic potential energy, k_{B} is the Boltzmann constant, and T as the temperature. The probability density of the system at time t within the subspace of the CVs is expressed as $\rho(\mathbf{z}; t)$. The forward propagation step ($\mathbf{z} \to \mathbf{z}'$) of the probability density from the time t to the time $t + \tau$ is,[38]

$$\rho(\mathbf{z}';t+\tau)=\int d\mathbf{z}\,\mathscr{P}_{\tau}(\mathbf{z}'\mid\mathbf{z})\;\rho(\mathbf{z};t) \tag{2}$$

where the propagator $\mathscr{P}_{\tau}(\mathbf{z}'\mid\mathbf{z})$ represents the transition from $\mathbf{z}$ to $\mathbf{z}'$ (n.b., forward time propagation is represented according to the right-to-left convention commonly used in chemical kinetics and quantum mechanics[49] rather than the left-to-right convention used in the field stochastic processes[50]). It is assumed that the dynamics within the reduced subspace of the CVs is Markovian with a finite time lag τ, and that the propagator (also called the transfer operator) obeys the Chapman-Kolmogorov equation, $\rho(t+n\tau)=\mathscr{P}_{n\tau}\cdot\rho(t)$, with $\mathscr{P}_{n\tau}=(\mathscr{P}_{\tau})^{n}$. It is assumed that the system is in equilibrium and that we have microscopic detailed balance, $\mathscr{P}_{\tau}(\mathbf{z}'\mid\mathbf{z})\rho_{\mathrm{eq}}(\mathbf{z})=\mathscr{P}_{\tau}(\mathbf{z}\mid\mathbf{z}')\rho_{\mathrm{eq}}(\mathbf{z}')$. Under these conditions, the effective propagator $\mathscr{P}_{\tau}(\mathbf{z}'\mid\mathbf{z})$ yields a self-consistent representation of the dynamics of the system within this subspace (closure of the dynamical propagation).

In practice, one should seek to determine the smallest possible time lag τ that achieves Markovianity for the effective propagator. An important framework to examine this issue is to rely on a spectral decomposition of the effective dynamical propagator.[9,38,51] The right-eigenfunction $\psi_{k}^{\mathrm{R}}(\mathbf{z})$ of the operator are defined as,[9,51]

$$\lambda_{k}\,\psi_{k}^{\mathrm{R}}(\mathbf{z}')=\int d\mathbf{z}\,\mathscr{P}_{\tau}(\mathbf{z}'\mid\mathbf{z})\,\psi_{k}^{\mathrm{R}}(\mathbf{z}) \tag{3}$$

where the eigenvalue $\lambda_{k}=e^{-\mu_{k}\tau}$. The eigenvalues depend on the time lag τ while the constants $\mu_{k}\geq 0$ represents associated τ-dependent intrinsic decay rate of the nth eigenmode. The eigenfunction $\psi_{1}^{\mathrm{R}}(\mathbf{z})$ with eigenvalue $\lambda_{1}=1(\mu_{0}=0)$ corresponds to the invariant equilibrium vector, $\rho_{\mathrm{eq}}(\mathbf{z})$. The eigenvalues are ordered from the slowest to the fastest process, i.e., $1=\lambda_{1}>\lambda_{2}>\lambda_{3}\ldots$, and $0=\mu_{1}<\mu_{2}<\mu_{3}\ldots$ There is also a set of associated orthogonal τ-dependent left-eigenfunctions

$$\lambda_{k}\,\psi_{k}^{\mathrm{L}}(\mathbf{z})=\int d\mathbf{z}'\psi_{k}^{\mathrm{L}}(\mathbf{z}')\mathscr{P}_{\tau}(\mathbf{z}'\mid\mathbf{z}) \tag{4}$$

with

$$\delta_{kl}=\int d\mathbf{z}\,\psi_{k}^{\mathrm{L}}(\mathbf{z})\,\psi_{l}^{\mathrm{R}}(\mathbf{z})=\left(\psi_{k}^{\mathrm{L}}\cdot\psi_{l}^{\mathrm{R}}\right) \tag{5}$$

Orthonormalization can also be expressed as,

$$\delta_{kl} = \int d\mathbf{z}\, \psi_k^{\mathrm{L}}(\mathbf{z})\, \psi_l^{\mathrm{L}}(\mathbf{z})\, \rho_{\mathrm{eq}}(\mathbf{z}) \tag{6}$$

using the relation $\psi_k^{\mathrm{R}}(\mathbf{z}) = \psi_k^{\mathrm{L}}(\mathbf{z})\rho_{\mathrm{eq}}(\mathbf{z})$, which follows from microscopic detailed balance.[52,53] We also have

$$\begin{aligned}\lambda_k\, \delta_{kl} &= \int d\mathbf{z} \int d\mathbf{z}' \psi_k^{\mathrm{L}}(\mathbf{z}')\mathscr{P}_\tau(\mathbf{z}' \mid \mathbf{z})\, \psi_l^{\mathrm{R}}(\mathbf{z}) \\ &= \int d\mathbf{z} \int d\mathbf{z}' \psi_k^{\mathrm{L}}(\mathbf{z}')\mathscr{P}_\tau(\mathbf{z}' \mid \mathbf{z})\, \psi_l^{\mathrm{L}}(\mathbf{z})\, \rho_{\mathrm{eq}}(\mathbf{z}) \\ &= \left\langle \psi_k^{\mathrm{L}}(\tau)\, \psi_l^{\mathrm{L}}(0) \right\rangle\end{aligned} \tag{7}$$

where $\langle \ldots \rangle$ represent an equilibrium average. The first right-eigenfunction is actually the equilibrium distribution, $\psi_1^{\mathrm{R}}(\mathbf{z}) = \rho_{\mathrm{eq}}(\mathbf{z})$, and its associated left-eigenfunction is uniformly equal to unity. Assuming that there are two metastable states A and B, then the second eigenvalue and associated eigenfunction should reflect the slow probability flux between A and B. The equilibrium time-correlation function of an arbitrary function $v(\mathbf{z})$ is,

$$\begin{aligned}\langle v(\tau)\, v(0) \rangle &= \int d\mathbf{z} \int d\mathbf{z}'\, v(\mathbf{z}')\mathscr{P}_\tau(\mathbf{z}' \mid \mathbf{z}) v(\mathbf{z})\, \rho_{\mathrm{eq}}(\mathbf{z}) \\ &= \sum_k \left(v \cdot \psi_k^{\mathrm{R}}\right)^2 e^{-\mu_k \tau}\end{aligned} \tag{8}$$

where

$$\left(v \cdot \psi_k^{\mathrm{R}}\right) = \int d\mathbf{z}\, v(\mathbf{z})\, \psi_k^{\mathrm{R}}(\mathbf{z}) \tag{9}$$

When $v(\mathbf{z})$ matches the slowest left-eigenfunction, $\psi_2^{\mathrm{L}}(\mathbf{z})$, then the time-correlation function, $\langle v(\tau)\, v(0) \rangle / \langle v(0)\, v(0) \rangle \approx \lambda_2$, reaches a maximum (the relaxation rate μ_2 reaches a minimum). This allows the formulation of a variational principle for the treatment of the spectral analysis.[48,54] Accordingly, a trial left-eigenfunction $v(\mathbf{z})$ can be variationally optimized by seeking to minimize the loss function $\mathscr{L}_v$,

$$\mathscr{L}_v = -\frac{\langle v(\tau)\, v(0) \rangle}{\langle v(0)\, v(0) \rangle} \tag{10}$$

A more general treatment can be formulated by expressing the trial left-eigenfunction $v(\mathbf{z})$ as a linear combination of M basis functions $v(\mathbf{z}) = \sum_{i=1}^{M} b_i F_i(\mathbf{z})$ with M unknown coefficients

b_i to be determined. Seeking the minimum of eq 10 with respect to the basis set coefficients, $\partial \mathscr{L}_v / \partial b_i = 0$, leads to the generalized eigenvalue problem,[55,56]

$$\mathbf{C}(\tau)\mathbf{B} = \mathbf{C}(0)\mathbf{B}\mathbf{\Lambda} \tag{11}$$

where the elements in $\mathbf{C}(\tau)$ and $\mathbf{C}(0)$ are equilibrium averages defined as $C_{ij}(\tau) = F_i(\tau)F_j(0)$ and $C_{ij}(0) = F_i(0)F_j(0)$, respectively. The expansion coefficients of the left-eigenfunctions $\psi_k^{\mathrm{L}}(\mathbf{z})$ are in the matrix $\mathbf{B}$, and the associated eigenvalues are in the diagonal matrix $\mathbf{\Lambda} \equiv \mathrm{diag}(\lambda_1, \lambda_2, \ldots)$. In the more general case, we will treat $F_i(\mathbf{z})$ as unknown kernel functions that will also need to be optimized. In the following, the optimal left-eigenfunctions $\psi_2^{\mathrm{L}}(\mathbf{z})$ will be referred to as the "learned CV" $\xi(\mathbf{z})$, which is essentially a model of the RC for the $A \leftrightarrow B$ slow transitions.

A different approach to characterize the kinetics of a slow process proceeds from TPT, the starting point being the forward committor $q(\mathbf{z})$ probability, which is the sum of the probability over all paths starting at $\mathbf{z}$ that ultimately reach the state B before ever reaching the state A.[31–34,38] The probability of each of these paths is expressed as a product of discrete propagation steps $\mathscr{P}_{n\tau} = \mathscr{P}_\tau \cdots \mathscr{P}_\tau$ with time lag τ, under the restriction that the intermediate states resulting from all these steps are not in A or B. It follows that $q(\mathbf{z})$ is written explicitly as,[38]

$$q(\mathbf{z}) = \int d\mathbf{z}' q(\mathbf{z}') \mathscr{P}_\tau(\mathbf{z}' \mid \mathbf{z}) \tag{12}$$

with the constraints $q(\mathbf{z}) = 0$ if $\mathbf{z} \in A$, and $q(\mathbf{z}) = 1$ if $\mathbf{z} \in B$. By construction, $0 \leq q(\mathbf{z}) \leq 1$. While the equations for the committor probabilities involve only the elementary propagator $\mathscr{P}_\tau(\mathbf{z}' \mid \mathbf{z})$ for the time lag τ, the fundamental validity of these equations is predicated upon the necessity to satisfy Markovity of the dynamics as expressed by the Chapman-Kolmogorov equation, $\mathscr{P}_{n\tau} \equiv (\mathscr{P}_\tau)^n$. The steady-state unidirectional reactive flux, J_{AB}, is given by,

$$J_{AB} = \frac{1}{2\tau}\left\langle (q(\tau) - q(0))^2 \right\rangle \tag{13}$$

The expression for J_{AB} can serve as a robust variational principle to optimize a trial committor $q(\mathbf{z}')$.[38,44,45] Minimizing the quantity J_{AB} with respect to the trial function $q(\mathbf{z})$ recovers eq 12 that formally defines the committor probability. Thus, defining the committor time-correlation function $C_{qq}(t) = (q(t) - q(0))^2/2$, one can use the loss function to refine a trial model function for the committor probability,

$$\mathscr{L}_q = \boldsymbol{C}_{qq}(\tau) \tag{14}$$

The committor $q(\mathbf{z})$ can also serve as a model of the RC for the $A \leftrightarrow B$ slow transitions.

The loss functions of eq 10 and eq 14, for the eigenfunction-based spectral analysis and the committor-based reactive flux analysis, respectively, are related. Both approaches seek to determine a one-dimensional reaction coordinate that represents the slow dynamics of the system on a long timescale. While the committor $q(\mathbf{z})$ is not quite equal to the left-eigenvector of the effective propagator, a useful approximate construction can be written as,[52]

$$q(\mathbf{z}) \approx -\left(\frac{a}{b-a}\right)\psi_1^{\mathrm{L}}(\mathbf{z}) + \left(\frac{1}{b-a}\right)\psi_2^{\mathrm{L}}(\mathbf{z}) \tag{15}$$

where $\psi_1^{\mathrm{L}}(\mathbf{z}) = 1$, $a = \psi_2^{\mathrm{L}}(\mathbf{z})$ with $\mathbf{z} \in A$, and $b = \psi_2^{\mathrm{L}}(\mathbf{z})$ with $\mathbf{z} \in B$, where $a = -(b-a)p_B$, and $1 = (b-a)^2(p_A p_B - \langle q(1-q)\rangle)$. This construction makes a function $q(\mathbf{z})$ that is equal to 0 for $\mathbf{z} \in A$, equal to 1 for $\mathbf{z} \in B$, and which approximately satisfies the backward propagation condition of eq 12,

$$\begin{aligned}
&\int d\mathbf{z}'\, q(\mathbf{z}')\mathscr{P}_\tau(\mathbf{z}' \mid \mathbf{z}) = -\left(\frac{a}{b-a}\right)\int d\mathbf{z}'\psi_1^{\mathrm{L}}(\mathbf{z}')\mathscr{P}_\tau(\mathbf{z}' \mid \mathbf{z}) + \left(\frac{1}{b-a}\right)\int d\mathbf{z}'\psi_2^{\mathrm{L}}(\mathbf{z}')\mathscr{P}_\tau(\mathbf{z}' \mid \mathbf{z}) \\
&= -\left(\frac{a}{b-a}\right)\psi_1^{\mathrm{L}}(\mathbf{z}) + \left(\frac{1}{b-a}\right)\lambda_2\,\psi_2^{\mathrm{L}}(\mathbf{z}) \\
&= q(\mathbf{z}) + \left(\frac{\lambda_2 - 1}{b-a}\right)\psi_2^{\mathrm{L}}(\mathbf{z}) \\
&\approx q(\mathbf{z})
\end{aligned} \tag{16}$$

where $|(\lambda_2 - 1)/(b-a)| \ll 1$. The critical difference is that the functional form of the eigenfunction-based reaction coordinate determined via eq 10 is unconstrained, whereas the committor in eq 14 is constrained in the two metastable states A and B.

2.2 Siamese neural networks

2.2.1 Using SRVs for collective-variable discovery—

To identify the slowest decorrelating mode of the molecular process at hand, we turn to the state-free reversible version of VAMPnets, or SRVs, with a SNN architecture,[57,58] as depicted in Figure 1. In a nutshell, an SNN consists of two sub-NNs of identical architecture, that is, the same number of hidden layers and neurons per hidden layer, sharing the same parameters, specifically the weights and biases, and activation functions. It ought to be noted that use is made here of an SNN architecture to avoid possible ambiguities in the theoretical discussion. In an actual software implementation, the SNN can be simplified (see the Supporting Information for more detail). The two sub-NNs are used to model the M unknown kernel functions $F_1(\mathbf{z}), \cdots, F_M(\mathbf{z})$, and fed with the MD trajectory with and without a time lag, τ. The spectral

decomposition of the Markov propagator is achieved by solving the generalized eigenvalue problem from eq 11, $\mathbf{C}(\tau)\mathbf{B} = \mathbf{C}(0)\mathbf{B}\mathbf{\Lambda}$. In practice, the elements of the matrices $\mathbf{C}(\tau)$ and $\mathbf{C}(0)$ are calculated as,[9]

$$C_{ij}(\tau) = \frac{1}{(N_t - N_\tau)} \sum_{n=1}^{N_t - N_\tau} F_i((n + N_\tau)\Delta t) F_j(n\Delta t) + \frac{1}{(N_t - N_\tau)} \sum_{n=N_\tau+1}^{N_t} F_i((n - N_\tau)\Delta t) F_j(n\Delta t) \tag{17}$$

and

$$C_{ij}(0) = \frac{1}{(N_t - N_\tau)} \sum_{n=1}^{N_t - N_\tau} F_i((n + N_\tau)\Delta t) F_j((n + N_\tau)\Delta t) + \frac{1}{(N_t - N_\tau)} \sum_{n=N_\tau+1}^{N_t} F_i((n - N_\tau)\Delta t) F_j((n - N_\tau)\Delta t) \tag{18}$$

where it is implied that the time dependence of the functions arises from the trajectory in Carterian coordinates via the CVs, i.e., $F_i(t) = F_i(\mathrm{z}(\mathrm{x}(t)))$. Δt is the time interval for discretizing the trajectory, N_t is the number of snapshots along the trajectory, and $\tau = N_\tau \Delta t$ corresponds to the time-lag. It should be noted that the matrices are constructed in a symmetrized fashion to improve numerical stability. The loss function of the SNN associated to the SRVs in our implementation is defined as $-\sum_{i=1}^{M} \lambda_i^2$, which is tantamount to the negative of total kinetic variance,[59] and can be considered as a generalization of eq 10 in the multidimensional cases. After optimizing this loss function, the slow decorrelating modes, mathematically represented as the eigenfunctions, are inferred as linear combinations of the components of the basis functions, F_i.

The eigenfunctions are sometimes called the “learned CVs”. In the present contribution, since our objective is to compare the properties of the committor function with those of the slowest decorrelating CV for a simple, two-state molecular process, the dimension of the latent space of our NN will be reduced to one.

2.2.2 Using VCNs for collective-variable discovery—Data-driven discovery of the committor probability, q, rests on an NN architecture similar to that described in the previous section, albeit with a latent space of dimension equal to one (see Figure 1). The main difference resides in the loss function, embodied in eq 14, and the identification of a scalar function, namely q, as opposed to a multidimensional function in the case of learned CVs. In addition, optimization of the committor probability following a variational principle incorporates two end-state boundary conditions, such that $q(\mathbf{z}(\mathbf{x})) = 0$ when $\mathbf{z}(\mathbf{x}) \in A$, $q(\mathbf{z}(\mathbf{x})) = 1$ when $\mathbf{z}(\mathbf{x}) \in B$, and $q(\mathbf{z}(\mathbf{x})) = F(\mathbf{z}(\mathbf{x}))$ elsewhere. The quantity $q(t)$, which appears in eq 13 and eq 14, is then computed as,

$$q(t) = \begin{cases} 0, & \mathbf{z}(t) \in A \\ 1, & \mathbf{z}(t) \in B \\ F(\mathbf{z}(t)), & \mathbf{z}(t) \notin (A \cup B) \end{cases}$$

(19)

In practice, we treat the metastable states A and B as absorbing states, which implies that for any short trajectory from $\mathbf{z}(t)$ to $\mathbf{z}(t+\tau)$, if any configuration sampled corresponds to either A, or B, then $q(t+\tau)=0$, or 1, respectively. In contrast with the discovery of CVs with SRVs, our implementation for the discovery of the committor probability obviates the need for solving an eigenvalue problem.

2.3 Biased simulations and enhanced sampling

To enhance sampling and accelerate the slow molecular process that underlies the transitions of interest, it may be necessary to introduce a biasing potential to the simulation to flatten the free-energy landscape. However, while adopting such a strategy, it is critical to have the ability to extract unbiased estimators of the key quantities that enter the analysis elaborated in subsection 2.2. This is especially critical in the case of time-correlation functions that enter the analysis in eq 10 and eq 14.

A practical approximation can be derived by assuming that the system at hand can be represented as a jump-like process on a discrete-state Markov model, in which the probability of the transition $\mathbf{z}\equiv\{z_1,\ldots,z_i,\ldots,z_n\}\rightarrow\mathbf{z}'\equiv\{z_1,\ldots,z_i+\Delta z,\ldots,z_n\}$ with time lag τ is expressed as,[60,61]

$$\begin{aligned}\mathscr{P}_\tau(\mathbf{z}'\mid\mathbf{z})&=\left(\tau\frac{D(\mathbf{z})+D(\mathbf{z}')}{2(\Delta z)^2}\right)\mathrm{e}^{-[W(\mathbf{z}')-W(\mathbf{z})]/2k_\mathrm{B}T}\\&=\mathrm{e}^{-W(\mathbf{z}')/2k_\mathrm{B}T}\left(\tau\frac{D(\mathbf{z})+D(\mathbf{z}')}{2(\Delta z)^2}\right)\mathrm{e}^{+W(\mathbf{z})/2k_\mathrm{B}T}\end{aligned}$$

(20)

Here, $D(\mathbf{z})$ is the position-dependent diffusion coefficient and $W(\mathbf{z})$ is the potential of mean force (PMF) in the subspace of the CVs. The jump-like process expressed by eq 20 reduces to the familiar Smoluchowski equation in the limit of $\Delta z\rightarrow 0$.[60,61] By virtue of this simple construct, the transition probability is affected by a perturbation biasing potential, $\delta W(\mathbf{z})$, as,

$$\mathscr{P}_\tau^{(\mathrm{p})}(\mathbf{z}'\mid\mathbf{z})=\mathrm{e}^{-\delta W(\mathbf{z}')/2k_\mathrm{B}T}\,\mathscr{P}_\tau(\mathbf{z}'\mid\mathbf{z})\,\mathrm{e}^{+\delta W(\mathbf{z})/2k_\mathrm{B}T}$$

(21)

It follows that the unbiased time-correlation function, $\langle f(\tau)\,g(0)\rangle$, in the unperturbed system, can be expressed in terms of the biased time-correlation function calculated in the perturbed system as,

$$\langle f(\tau)\,g(0)\rangle=\left\langle\mathrm{e}^{+\delta W/k_\mathrm{B}T}\right\rangle_{(\mathrm{p})}^{-1}\left\langle f(\tau)\,\mathrm{e}^{+\delta W(\tau)/2k_\mathrm{B}T}\,g(0)\,\mathrm{e}^{+\delta W(0)/2k_\mathrm{B}T}\right\rangle_{(\mathrm{p})}$$

(22)

This approximation for unbiasing a time-correlation function is akin to the simple prescription used previously by several authors,[29,62] but is different from the dynamic

histogram analysis method, which assumes a discretization of the metastable states.[63] In the present work, it is used to calculate the unbiased time-correlation functions of eq 10 and eq 14 for the SRVs and committor treatments using biased simulations.

Different strategies are available to construct an effective perturbation, $\delta W(\mathbf{z})$, within the subspace of the CVs to improve sampling of slow $A \leftrightarrow B$ transitions. When dealing with a system with two prominent metastable states, a particularly effective approach to enhance the sampling along the conformational transition pathway linking them can be built upon the string method.[64–66] A string pathway consists of a one-dimensional chain of $K+1$ copies of the system, also called "images", in the subspace of the CVs, $\left\{\mathbf{z}^{(0)}, \mathbf{z}^{(1)}, \ldots, \mathbf{z}^{(K)}\right\}$ that progressively goes from the state A to the state B.[67–69] The string can serve to define the progress variable s, referred to as path collective variable (PCV),[70]

$$s(\mathbf{z}) = \frac{\sum_{k=0}^{K} \left(\frac{k}{K}\right) \mathrm{e}^{-\alpha\left(\mathbf{z}-\mathbf{z}^{(k)}\right)^2}}{\sum_{k=0}^{K} \mathrm{e}^{-\alpha\left(\mathbf{z}-\mathbf{z}^{(k)}\right)^2}} \tag{23}$$

Since $s(\mathbf{z})$ is a differentiable function of the CVs, $\mathbf{z}$, it is amenable to adaptive biasing force[71,72] (ABF) free-energy calculations. In principle, the one-dimensional free-energy profile, or PMF, along s reflects the correct equilibrium probability of the configurations. It is, however, important to note that, in practice, to be truly useful, the function $s(\mathbf{z})$ needs not be a perfect model of the RC. For as long as it reasonable connects the two end-states and passes through the kinetic bottleneck—or saddle point—along the transition pathway, the function $s(\mathbf{z})$ can serve as an effective progress variable to support an enhanced-sampling strategy leaning on biased simulations. If needed, one may also introduce additional biasing along the orthogonal variable,

$$\zeta(\mathbf{z}) = -\frac{1}{\alpha} \ln \sum_{k=0}^{K} \mathrm{e}^{-\alpha\left(\mathbf{z}-\mathbf{z}^{(k)}\right)^2} \tag{24}$$

to further control the enhanced sampling. Alternative path-following variables have also been considered based on more complicated functional forms.[73,74] By construction, eq 23 does not automatically yield a physically reasonable order parameter of the conformational transition from A to B. For example, there are serious issues if the images are scrambled. However, if the images are adequately ordered to represent the progress of the transition from A to B in a meaningful fashion, and a suitable value for α is chosen, then variable $s(\mathbf{z};\alpha)$ will vary smoothly from 0 to 1.[45] In the applications described hereafter, the biasing potential, $\delta W(s)$, was only applied with respect to the variable s, with $1/\alpha$ chosen to be equal to the mean squared distance between adjacent images.

3 Computational details

In this section, we detail the algorithm developed to learn the committor function from biased trajectories, using an SNN,[57] and compare this algorithm with the SRVs[28] put forth to learn CVs, leaning on a similar NN architecture. It ought to be noted that the learned CVs can be iteratively improved through the following workflow:[26] (i) sampling along a large set of candidate CVs, employing a computationally efficient, albeit approximate free-energy method, such as extended generalized adaptive biasing force (egABF)[75] (ii) learning a small set of new CVs from the biased trajectories from the previous step, (iii) sampling along the new CVs using an accurate free-energy method, such as well-tempered meta-extended ABF (WTM-eABF),[76] and (iv) going back to step (ii) until the free-energy calculation is converged. Since the unbiased time-correlation function can be computed by the reweighting approach embodied in eq 22, it is also possible to use a similar iterative strategy to learn the committor probability from biased trajectories. Moreover, since the committor is, by definition, a one-dimensional scalar function, to save computational resources and speedup the convergence, one could focus sampling along a string, by means of PCV $s(\mathbf{z})$[70] as defined in eq 23—as opposed to an extensive sampling along $q(\mathbf{z})$, which may span the entire subspace of the CVs. Here, the string is a committor-consistent one, orthogonal to the isocommittor surfaces folliating the reaction pathway, as obtained in the committor-consistent string variational method (CCVSM).[45] In other words, the two cruxes to close the loop for an iterative strategy with VCNs are (a) learning the latter scalar function from a biased trajectory along $\tilde{s}(\mathbf{z})$, and (b) obtaining a committor-consistent string from the learned committor probability. In this contribution, the simplicity of the models utilized to illustrate the methodology applied to the exploration of transitions between two metastabile states obviates the need for additional iterations.

As shown in Figure 1, the SNN features two identical sub-NNs, which work in tandem on two different input datasets, namely the trajectory $\mathbf{z}(t)$ and its time-lagged counterpart $\mathbf{z}(t+\tau)$, respectively. For comparison purposes, unless stated otherwise, the sub-NNs used in this contribution consist of four intermediate exponential linear unit (ELU)[77] layers containing each 32 neurons, or computational units, and the linear output layer containing one neuron. The number of neurons in the input layer depends on the number of candidate CVs. In the course of training, the original data set was divided into a training set and a validation set, in a 9:1 proportion. In each training iteration, or epoch, the training set was randomly split into batches of size $\lfloor N_{\text{train}}^{0.5} \rfloor$, where $N_{\text{train}}^{0.5}$ is the number of samples in the training set and $\lfloor \ldots \rfloor$ is the floor function, fed into the sub-NNs for the calculation of the values of the loss function. The NN parameters were then optimized by the Adam optimizer[78] to minimize the average loss. In order to avoid overfitting, training was stopped if the loss of the validation set did not decrease within ten epochs (early stopping). The time lag, τ, was chosen to be 0.5 ns. The trajectories were 100-ns long for each of three illustrative models, namely the simulations of a carbon atom on (i) a one-dimensional double-well potential, (ii) the two-dimensional Müller-Brown potential,[79] and (iii) the two-dimensional Berezhkovskii-Szabo potential,[80] with anisotropic diffusion. The length of the trajectory of the isomerization of N-acetyl-N′-methylalanylamide (NANMA, also commonly known as alanine dipeptide—or dialanine) in vacuum is equal to 500 ns. For the

biased simulations, since $\delta W(\mathbf{z})$ is required to be converged for the estimation of the weights acccording to eq 22, the first 25 ns of each trajectory were discarded.

The simulations of the one-dimensional double-well potential, the Müller-Brown potential and the isomerization of NANMA were carried out using NAMD 2.14[81] with the Colvars module.[82] The two-dimensional Berezhkovskii-Szabo potential with anisotropic diffusion was simulated, employing an in-house code (available from the authors upon request). To illustrate the learning of the committor probabilities from biased simulations, in the Müller-Brown potential and the Berezhkovskii-Szabo potential cases, the WTM-eABF trajectories along $s(\mathbf{z})$ were used. The corresponding strings were constructed from the minimum free-energy pathways (MFEPs) determined by the Dijkstra algorithm.[83] We also succeeded to calculate the transition rates k_{AB} (see section 4 of Supporting Information for more detail), employing biased trajectories of the one-dimensional double-well potential, the Müller-Brown potential, the two-dimensional Berezhkovskii-Szabo potential, and the potential underlying the isomerization of NANMA, with the reweighting scheme of eq 22, assuming short time lags. In the NANMA case, use was made of a WTM-eABF biased trajectory along the ϕ and ψ backbone dihedral angles. NANMA was described by the CHARMM22 force field,[84] and the temperature of the simulation was kept at 300K using Langevin dynamics.

4 Results

4.1 One-dimensional double-well potential

The first prototypical illustration examined here is the one-dimensional double-well potential depicted in Figure 2A, and defined as,

$$V(x) = -4e^{-(x+2)^2} - 4e^{-(x-2)^2} + 4 \tag{25}$$

where the regions around the two basins, namely $-2.54\,\mathring{A} < x < -1.46\,\mathring{A}$ and $+1.46\,\mathring{A} < x < +2.54\,\mathring{A}$, are marked as the two metastabile states, respectively. x is the atomic coordinate along the abscissa. The units of x and $V(x)$ are Å and kcal/mol, respectively. We chose x as the input variable of the NNs, namely $z \equiv x$ in this case. Detail of the simulation and the calculation of the transition rates between the two metastable states can be found in the Supporting Information. The learned committor probabilities, $q(x)$, and CVs, $\xi(x)$, from biased and unbiased simulations along x are shown in Figure 2B and Figure 2C, respectively. If the reweighting scheme embodied in eq 22 is employed, then the learned $q(x)$ (orange line in Figure 2B) is in quantitative agreement with the unbiased result (blue line in Figure 2B), and both results feature smooth transitions from the two metastable states to the barrier at $x = 0$. Conversely, if the bias is ignored and no reweighting is applied, then the result (green line in Figure 2B) bears no resemblance with the unbiased result. Moreover, the transition from the metastable states to the barrier is not smooth. Comparing the results from CV discovery using the unbiased simulation (blue in Figure 2C), and the biased simulation with reweighting (orange in Figure 2C) and without reweighting (green in

Figure 2C), there is a clear resemblance in $\xi(x)$ from the unbiased simulation and the biased one with proper reweighting, and both of them are flat in the two metastable states. It is interesting that although the two metastabile states are not explicitly labeled in the learning of $\xi(x)$, as they are in the learning of $q(x)$, they are still adequately identified. Conversely, the variable $\xi(x)$ learned without reweighting is nearly proportional to x, and fails to render a proper depiction of the two metastable states. We can also observe similarities in the learned $q(x)$ and $\xi(x)$. At first glance, when training from the unbiased trajectory or the biased one with appropriate reweighting, the committor, $q(x)$, correlates almost linearly with the slowly-decorrelating variable, $\xi(x)$, which is in line with eq 15. Indeed, there are only two basins and one slow-relaxation mode in our toy model. It is, therefore, is not surprising that $q(x)$ coincides with $\xi(x)$. It ought to be noted, however, that the learning of $\xi(x)$ is similar to a blind separation of metastable states without extra labeling. If there are more than two metastable states in the free-energy landscape, then the learned CV, $\xi(x)$, may not be able to separate exactly the two metastable states as desired.

4.2 Müller-Brown two-dimensional potential

The second prototypical illustration examined in the present contribution is the two-dimensional Müller-Brown potential,,[79] which has served as a prototypical model for developing new methods, and has been studied extensively.[15,85–87] The potential energy function, $V(x, y)$, is defined as,

$$V(x,y) = k \sum_{i=1}^{4} d_i \, \mathrm{e}^{a_i(x-x_i)^2 + b_i(x-x_i)(y-y_i) + c_i(y-y_i)} \tag{26}$$

where the constants take the following values, $k = 0.05$, $[d_1, d_2, d_3, d_4] = [-200, -100, -170, 15]$, $[a_1, a_2, a_3, a_4] = [-1, -1, -6.5, 0.7]$, $[b_1, b_2, b_3, b_4] = [0, 0, 11, 0.6]$, $[c_1, c_2, c_3, c_4] = [-10, -10 - 6.5, 0.7]$, $[x_1, x_2, x_3, x_4] = [1, 0, -0.5, -1]$ and $[y_1, y_2, y_3, y_4] = [0, 0.5, 1.5, 1]$. x and y are the atomic coordinates along the abscissa and the ordinate, respectively. The units of x, y and $V(x)$ are Å, Å and kcal/mol, respectively. Both x and y were chosen as the input variables of the NNs, namely $\mathbf{z} \equiv [x, y]$. The two metastable states are defined as the point sets $\{(x, y) \mid x \in (-1.0, -0.02), y \in (1.0, 2.0), V(x, y) < 1.0\}$ and $\{(x, y) \mid x \in (0.2, 1.0), y \in (-0.2, 0.2), V(x, y) < 3.0\}$, respectively. The detail of the calculation of the transition rates between the two metastable states can be found in the Supporting Information. The biased trajectory was obtained from a WTM-eABF simulation along the MFEP (shown as green lines in Figure 3A, B, D and E).[83] The projections of the learned $q(x, y)$ onto (x, y) from the unbiased trajectory and the biased one with appropriate reweighting are shown in Figure 3A and Figure 3B, respectively. In both instances, the $q(x, y) = 0.5$ isosurfaces go through the barrier, and the committor probabilities along the MFEP (Figure 3C) are similar, indicating that the transition between the two metastable states are well captured. In addition, we note that the $\xi(x, y) = 0$ isosurfaces from an unbiased trajectory (Figure 3D) and a biased one with the reweighting embodied in eq 22 (Figure 3E) also go through the barrier. If the positions of the two metastable states

cannot be determined, then the boundary conditions of $q(x, y)$ will be missing. Under these circumstances, the similarity between $q(x, y)$ and $\xi(x, y)$ enables us to approximate $q(x, y)$ by $\xi(x, y)$.

In addition, to assess whether the committor isosurface could be potentially improved via an iterative approach, we have learned $q(x, y)$ for this potential with VCNs, using two biased trajectories obtained from WTM-eABF simulations along PCVs, and based on (i) a physically meaningful pathway (the MFEP), and (ii) an unphysical one. Unsurprisingly, learning from the biased trajectory along the PCV constructed from this unphysical pathway supplies a less accurate committor isosurface (see Figure S8 of the Supporting Information). Nonetheless, the latter remains qualitatively correct, indicating that an imperfect information could be used to improve progressively the initial pathway, and learn a more accurate representation of the committor isosurface.

4.3 Berezhkovskii-Szabo two-dimensional potential

To investigate whether the learned committor probabilities and CVs can reflect the effect of anisotropic diffusion, as observed with the CCVSM,[45] we trained the NNs, using both the unbiased and biased trajectories with the Berezhkovskii-Szabo potential,[80] under three distinct conditions, namely $D_y/D_x = \delta = 0.1$, 1.0, and 10.0, where D_y and D_x are the diffusivities along the ordinate and the abscissa, respectively. The Berezhkovskii-Szabo potential is defined as,

$$\beta V(x, y) = \beta V(x) + 1.01\omega^2(x - y)^2/2 \tag{27}$$

where $V(x)$ is calculated from,

$$\beta V(x) = \begin{cases} -\omega^2 x_0^2/4 + \omega^2(x + x_0)^2/2, & x < -x_0/2 \\ -\omega^2 x^2/2, & -x_0/2 \le x \le x_0/2 \\ -\omega^2 x_0^2/4 + \omega^2(x - x_0)^2/2, & x_0/2 < x \end{cases} \tag{28}$$

where β is equal to $(k_B T)^{-1}$, ω^2 is 4 and x_0 is 2.2 Å, respectively. T was chosen to 300K in our simulations. The units of x, y and $V(x)$ are Å and kcal/mol, respectively. Both x and y were chosen as the input variables of the NNs, namely $\mathbf{z} \equiv [x, y]$. The details of the simulations and transition rates are attached in the Supporting Information.

The projections of $q(x, y)$ and $\xi(x, y)$ onto (x, y) in different diffusive conditions obtained from the unbiased trajectories are gathered in Figure 4. Similar to the results reported for the CCVSM,[45] we observe that the $q(x, y) = 0.5$ isosurface is nearly parallel to the abscissa when δ is equal to 0.1 (Figure 4A), nearly parallel to the ordinate when δ is equal to 10.0 (Figure 4C), and nearly orthogonal to the MFEP when δ is equal to 1.0 (Figure 4B). These results strongly suggest that the committor probabilities learned from our NN models correctly

capture the underlying kinetics, just like those obtained with the CCVSM. Similarly, the CVs learned from SRVs, as shown in Figure 4E, Figure 4F, and Figure 4G, are also able to capture the effect of anisotropic diffusion. The isosurfaces $\xi(x, y) = 0$ follow the same patterns in the three different diffusive conditions as the isosurfaces $q(x, y) = 0.5$, which further reinforces the idea that $\xi(x, y)$ could be used to approximate $q(x, y)$, as previously shown for the Müller-Brown potential.

The projections of $q(x, y)$ and $\xi(x, y)$ onto the (x, y)–plane obtained from the WTM-eABF biased trajectories along a string with our reweighting scheme are shown in Figure 5, and resemble the results from the unbiased simulation, as depicted in Figure 4. It can be inferred from the similarity between the biased results and the unbiased ones that, here again, the kinetic information is adequately recovered from biased trajectories, assuming proper reweighting.

4.4 Isomerization of N-acetyl-N′-methylalanylamide

As a final example of biological relevance, we employed VCNs to investigate the transition between the C_{7eq} and C_{7ax} conformations of NANMA in vacuum (see Figure S8 for a reference free-energy landscape). Due to the periodic nature of the backbone dihedral angles, ϕ and ψ, we used $\sin\phi$, $\sin\psi$, $\cos\phi$ and $\cos\psi$ as the input features of the NNs. As shown in Figure 6A, the learned committor, $q(\phi, \psi)$, from a 500-ns long unbiased trajectory is able to highlight the two saddle points, $(\phi, \psi) = (0^\circ, -67.5^\circ)$ and $(135°, -115°)$, on the possible transition pathways, which is in agreement with previous studies,[34,70,88] wherein isomerization of NANMA was examined using PCV free-energy calculations.

The learned committor from a 150-ns WTM-eABF biased trajectory with appropriate reweighting (Figure 6B) also features similar isosurfaces, which means that learning the committor probabilities from a shorter biased trajectory could achieve almost the same accuracy in the identification of the transitions as learning from a long unbiased trajectory. We further shortened both the biased and unbiased trajectories used for training and found that the committor learned from a 2.5-ns biased trajectory was able to discriminate the C_{7eq} and C_{7ax} metastable states, while the one learned from an unbiased trajectory of the same length could not, as shown in Figure S1. The committor learned from an unbiased trajectory succeeded to discriminate the metastable states only at the price of extending the trajectory to 10 ns. In addition, we compared the learned CV from SRVs using the same NN parameters with the learned committor, and found that the former can also discriminate the C_{7eq} and C_{7ax} metastable states,[89] and identify the transitions. The similarity of the learned CV and the learned committor from both biased and unbiased trajectories was measured using linear regression, and the coefficients of determination are all close to 1, as shown in Table S1 in the Supporting Information, indicating that the learned CV and the learned committor are highly linear correlated.

4.5 Determination of transition rates

The transition rates are determined assuming a dynamical system with two long-lived metastable states, A and B,

$$A \underset{k_{BA}}{\overset{k_{AB}}{\rightleftharpoons}} B$$

The overall decay rate of the system is $k_{AB} + k_{BA}$, and the equilibrium state probabilities are $p_A = k_{BA}/(k_{AB} + k_{BA})$ and $p_B = k_{AB}/(k_{AB} + k_{BA})$. At equilibrium, the total unidirectional fluxes are equal, with $J_{AB} = p_A k_{AB} = J_{BA} = p_B k_{BA}$. The mean first-passage times (MFPT) from A to B and from B to A are $1/k_{AB}$ and $1/k_{BA}$, respectively.[37]

In SRVs, the eigenvalue of the slowest eigenmode of interest is $\lambda_2 = e^{-\mu_2 \tau}$, where μ_2 represents the overall decay rate or relaxation rate, which can be determined through $\mu_2 = -\ln \lambda_2(\tau)/\tau$.[48] The transition rate from A to B is $k_{AB} = \mu_2 p_B$. With VCNs, the transition rate from A to B can be determined from the unidirectional reactive flux $J_{AB} = C_{qq}(\tau)/\tau$ defined in eq 13 in terms of the committor time-correlation function $C_{qq}(\tau)$.[38] The transition rate from A to B is $k_{AB} = J_{AB}/p_A$. For both approaches, the long-time behavior of the expression $f(\tau)/\tau$, where $f(\tau)$ stands for $-\ln \lambda_2(\tau)$ or $C_{qq}(\tau)$, was extracted from the plateau in the slope of the numerator $f(\tau)$ as a function of the time-lag τ.[44] The transition rates were also determined from the MFPTs using the unbiased trajectories to use as a reference to compare with the other estimates.

In practice, to estimate the rates from SRVs and VCNs, the trajectories of z were transformed to those of $\xi(\mathbf{z})$ and $q(\mathbf{z})$ with different time lags, respectively. The eigenvalues, $\lambda_k(\tau)$, and the time correlation function, $C_{qq}(\tau)$, were then evaluated, as described in section 2.2 and eq 14, respectively. The rate, k_{AB}, could be determined from either the slope of $-\ln \lambda_2(\tau)$ as a function of τ and p_B in SRVs, or the slope of $C_{qq}(\tau)$[44] as a function of τ and p_A within the framework of VCNs. When biased trajectories were employed, the slopes were determined using the end-point reweighting expression eq 22. (see Figure S2–S7 and section 4 of the Supporting Information for additional detail).

For all the systems, the transition rate k_{AB} was determined from the MFPT between A and B using unbiased trajectories, as well as from SRVs and VCNs, using both unbiased and biased trajectories. The results obtained for the one-dimensional double-well potential, the two-dimensional Müller-Brown potential, the two-dimensional Berezhkovskii-Szabo potential, and the potential underlying the isomerization of NANMA are gathered in Table 1

As can be seen in Table 1, the rates determined from SRVs and VCNs, using either unbiased or biased trajectories, can reproduce, albeit not perfectly, the reference quantities determined using mean first-passage times (MFPTs) from unbiased trajectories. It is likely that inaccuracies in the determination of the transition rate from the biased simulations are due to the limitations of the end-point reweighting based on eq 22.

5 Conclusion

In this contribution, we elaborated variational committor-based neural networks, or VCNs, for the determination of the committor probability using a SNN architecture to implement

the variational principle from the TPT framework.[30,38,44,45] The results from VCNs were compared to those from SRVs with an analogous SNN architecture.[27,28] A striking resemblance between the slowest decorrelating mode from SRVs and the learned committor from VCNs was observed for the illustrative models examined herein (see Table S1–S6 for a quantitative analysis). This resemblance is explained by the linear correlation between the committor probability and the slowest decorrelating mode in the case of a system with two metastable states,[52] thus highlighting the theoretical linkage between SRVs and VCNs.

It is of interest to consider the relative merits and drawbacks of SRVs and VCNs. What circumstances should motivate the usage of one over the other is a key question. Unlike SRVs, VCNs require prior knowledge of the two key metastable states, A and B, a foundational element of TPT.[30] In that sense, VCNs are more “hands-on”, involving some deliberate choices made by the end-user. In contrast, this information is not needed for SRVs, which are unsupervised. Such differences may have both good or bad consequences, depending upon the problem at hand. With VCNs, one must choose two meaningful metastable states, so that the learned committor will accurately capture the slowest eigenmode in the system as shown by eq 15. An incorrect choice of the metastable states is likely to yield a learned committor that is not useful. Nonetheless, if one knows with confidence the two states from experiment, which is often the case for complex biomolecular systems, then it makes sense to leverage this information and turn to VCNs. On the other hand, when the metastable states have not been identified, using the unsupervised SRVs may be more advantageous. The method aims at providing a complete and objective picture of a dynamical system through an unsupervised discovery of all the relevant metastable states. This is, however, truly an ambitious goal. Realistically, SRVs may fall short in the case of complicated biological processes. For example, the learned transitions may be kinetically slow, but may not be of biological relevance. Ultimately, SRVs and VCNs should be considered as complementary approaches. When employed judiciously, the two strategies used in combination can help better define the landscape underlying the slow transitions for a process of interest.[90]

Knowledge of the two metastable states could be exploited in the design of an iterative strategy. For example, an initial string could be constructed between the two states, and the committor can be learned from VCNs using one-dimensional biased trajectory along the PCV[70] based on this initial string. A new committor-consistent string could then be gradually improved by aligning its tangent with the gradient of the committor, $\nabla q(\mathbf{z})$, at each new iteration.[44,45] Although the simple examples reported here obviate the need for pursuing the optimization beyond the first iteration, multiple iterations are likely to be necessary in the case of more intricate molecular processes. It is noteworthy that such committor-consistent transition pathway is distinct from those obtained from traditional algorithms.[6–69] Conversely, as there is no available initial string, the iterative SRVs[26] approach could only use the biased trajectories along the learned CVs, which may require multidimensional free-energy calculations that have generally higher computational cost and slower convergence rates than the one-dimensional biased simulations along PCV based on strings.

We also illustrated an end-point reweighting scheme for extracting unbiased information from biased trajectories. The results show that meaningful models of both the committor inferred from VCNs and the slowest decorrelating mode extracted from SRVs could be constructed from SNNs trained from enhanced-sampling biased simulations, obviating the need for long, unbiased trajectories. The transition rate could be estimated from the biased trajectories with reasonable, albeit imperfect accuracy, owing to the limitation of the unbiasing scheme. Possible solutions to address this limitation will require more sophisticated unbiasing schemes.[45,91,92]

While the methodology reported herein was devised in the context of slow molecular processes, like rare conformational transitions, similar concepts may be effectively applied to improve the convergence of free-energy calculations of alchemical transformations. The latter are commonly carried out within the chemical subspace, controlled by the force-field parameters, as well as the so-called thermodynamic coupling parameters. Identifying the optimal reaction pathway along the slowest CV within this subspace of coupling parameters could help design a more efficient enhanced-sampling strategy for such alchemical free-energy calculations.

Lastly, while the data-driven strategy presented in this contribution has been illustrated with paradigmatic slow transitions, it is envisioned to be readily applicable to more intricate molecular processes, and to possibly significantly larger biological objects, yet at the price of increasing the complexity of the dense sub-NNs employed here, or of turning altogether to alternate classes of sub-NNs, better suited to address the problem at hand, like those employed in probabilistic learning.[19]

Supplementary Material

Refer to Web version on PubMed Central for supplementary material.

Acknowledgement

This work was supported by the Agence Nationale de la Recherche (ProteaseInAction and LOR-AI, C.C.), the National Science Foundation through grant grant MCB-1517221 (B.R.), and the France and Chicago Collaborating in The Sciences (FACCTS) program. The authors are indebted to Yihang Wang (University of Chicago) for insightful discussions.

References

(1). Hollingsworth SA; Dror RO Molecular Dynamics Simulation for All. Neuron 2018, 99, 1129–1143. [PubMed: 30236283]

(2). Chipot C, Pohorille A, Eds. Free Energy Calculations: Theory and Applications in Chemistry and Biology; Springer-Verlag, Berlin Heidelberg: Berlin, Germany, 2007.

(3). Lelievre T; Rousset M; Stoltz G Free Energy Computations: A Mathematical Perspective; Imperial College Press: London, 2010.

(4). Peters B Reaction Coordinates and Mechanistic Hypothesis Tests. Ann. Rev. Phys. Chem 2016, 67, 669–690. [PubMed: 27090846]

(5). Rogal J Reaction Coordinates in Complex Systems—a Perspective. Euro. Phys. J. B 2021, 94, 223.

(6). Chen H; Chipot C Enhancing Sampling with Free-Energy Calculations. Curr. Opin. Struct. Biol 2022, 77, 102497. [PubMed: 36410221]

(7). Liu P; Shao X; Chipot C; Cai W The True Nature of Rotary Movements in Rotaxanes. Chem. Sci 2016, 7, 457–462. [PubMed: 30155010]

(8). Naritomi Y; Fuchigami S Slow Dynamics in Protein Fluctuations Revealed by Time-Structure Based Independent Component Analysis: The Case of Domain Motions. J. Chem. Phys 2011–02, 134, 065101. [PubMed: 21322734]

(9). Wu H; Nüske F; Paul F; Klus S; Koltai P; Noé F Variational Koopman Models: Slow Collective Variables and Molecular Kinetics from Short Off-equilibrium Simulations. J. Chem. Phys 2017, 146.

(10). Tiwary P; Berne BJ Spectral Gap Optimization of Order Parameters for Sampling Complex Molecular Systems. Proc. Natl. Acad. Sci. U.S.A 2016, 113, 2839–2844. [PubMed: 26929365]

(11). Tsai ST; Smith Z; Tiwary P SGOOP-d: Estimating Kinetic Distances and Reaction Coordinate Dimensionality for Rare Event Systems from Biased/Unbiased Simulations. J. Chem. Theory Comput 2021, 17, 6757–6765. [PubMed: 34662516]

(12). McGibbon RT; Husic BE; Pande VS Identification of Simple Reaction Coordinates from Complex Dynamics. J. Chem. Phys 2017, 146.

(13). Sultan MM; Pande VS tICA-Metadynamics: Accelerating Metadynamics by Using Kinetically Selected Collective Variables. J. Chem. Theory Comput 2017, 13, 2440–2447. [PubMed: 28383914]

(14). Hooft F; Pérez de Alba Ortíz A; Ensing B Discovering Collective Variables of Molecular Transitions via Genetic Algorithms and Neural Networks. J. Chem. Theory Comput 2021, 17, 2294–2306. [PubMed: 33662202]

(15). Ramil M; Boudier C; Goryaeva AM; Marinica M-C; Maillet J-B On Sampling Minimum Energy Path. J. Chem. Theory Comput 2022, 18, 5864–5875. [PubMed: 36073162]

(16). Novelli P; Bonati L; Pontil M; Parrinello M Characterizing Metastable States with the Help of Machine Learning. J. Chem. Theory Comput 2022, 18, 5195–5202. [PubMed: 35920063]

(17). Chen W; Tan AR; Ferguson AL Collective Variable Discovery and Enhanced Sampling Using Autoencoders: Innovations in Network Architecture and Error Function Design. J. Chem. Phys 2018, 149, 072312. [PubMed: 30134681]

(18). Ribeiro JML; Bravo P; Wang Y; Tiwary P Reweighted Autoencoded Variational Bayes for Enhanced Sampling (RAVE). J. Chem. Phys 2018, 149, 072301. [PubMed: 30134694]

(19). Wang Y; Ribeiro JML; Tiwary P Past-Future Information Bottleneck Framework for Sampling Molecular Reaction Coordinate, Thermodynamics and Kinetics. Nature Comm. 2019, 10, 3573.

(20). Sidky H; Chen W; Ferguson AL Machine Learning for Collective Variable Discovery and Enhanced Sampling in Biomolecular Simulation. Mol. Phys 2020, 118, e1737742.

(21). Wang Y; Lamim Ribeiro JM; Tiwary P Machine Learning Approaches for Analyzing and Enhancing Molecular Dynamics Simulations. 2020, 61, 139–145.

(22). Bonati L; Piccini G; Parrinello M Deep Learning the Slow Modes for Rare Events Sampling. Proc. Natl. Acad. Sci. U.S.A 2021, 118, e2113533118. [PubMed: 34706940]

(23). Belkacemi Z; Gkeka P; Lelièvre T; Stoltz G Chasing collective variables using autoencoders and biased trajectories. J. Chem. Theory Comput 2022, 18, 59–78. [PubMed: 34965117]

(24). Kramer MA Autoassociative Neural Networks. Comput. Chem. Eng 1992, 16, 313–328.

(25). Wehmeyer C; Noé F Time-lagged autoencoders: Deep learning of slow collective variables for molecular kinetics. J. Chem. Phys 2018, 148, 241703. [PubMed: 29960344]

(26). Chen H; C. C Chasing Collective Variables Using Temporal Data-Driven Strategies. Quart. Rev. Biophys. Discovery 2023, 4, e2.

(27). Mardt A; Pasquali L; Wu H; Noé F VAMPnets for Deep Learning of Molecular Kinetics. Nat. Commun 2018, 9,5. [PubMed: 29295994]

(28). Chen W; Sidky H; Ferguson AL Nonlinear Discovery of Slow Molecular Modes Using State-Free Reversible VAMPnets. J. Chem. Phys 2019, 150, 214114. [PubMed: 31176319]

(29). Wang Y; Tiwary P Understanding the Role of Predictive Time Delay and Biased Propagator in RAVE. J. Chem. Phys 2020, 152, 144102. [PubMed: 32295373]

(30). E W; Vanden-Eijnden E Transition-path Theory and Path-finding Algorithms for the Study of Rare Events. Annu. Rev. Phys. Chem 2010, 61, 391–420. [PubMed: 18999998]

(31). Onsager L Initial Recombination of Ions. Phys. Rev 1938, 54, 554–557.

(32). Du R; Pande V; Grosberg A; Tanaka T; Shakhnovich E On the Transition Coordinate for Protein Folding. J. Chem. Phys 1998, 108, 334–350.

(33). Geissler P; Dellago C; Chandler D Kinetic Pathways of Ion Pair Dissociation in Water. J. Phys. Chem. B 1999, 103, 3706–3710.

(34). Bolhuis PG; Dellago C; Chandler D Reaction Coordinates of Biomolecular Isomerization. Proc. Natl. Acad. Sci. U. S. A 2000, 97, 5877–5882. [PubMed: 10801977]

(35). Berezhkovskii A; Hummer G; Szabo A Reactive Flux and Folding Pathways in Network Models of Coarse-grained Protein Dynamics. J. Chem. Phys 2009, 130, 205102. [PubMed: 19485483]

(36). Berezhkovskii AM; Szabo A Diffusion Along the Splitting/commitment Probability Reaction Coordinate. J. Phys. Chem. B 2013, 117, 13115–13119. [PubMed: 23777371]

(37). Berezhkovskii AM; Szabo A Committors, First-passage Times, Fluxes, Markov States, Milestones, and All That. J. Chem. Phys 2019, 150, 054106. [PubMed: 30736684]

(38). Roux B String Method with Swarms-of-Trajectories, Mean Drifts, Lag Time, and Committor. J. Phys. Chem. A 2021, 125, 7558–7571. [PubMed: 34406010]

(39). Bowman GR; Pande VS; Noé F An introduction to Markov state models and their application to long timescale molecular simulation; Springer Science & Business Media, 2013; Vol. 797.

(40). Faradjian AK; Elber R Computing Time Scales from Reaction Coordinates by Milestoning. J. Chem. Phys 2004, 120, 10880–10889. [PubMed: 15268118]

(41). Zuckerman DM; Chong LT Weighted Ensemble Simulation: Review of Methodology, Applications, and Software. Annu. Rev. Biophys 2017, 46, 43–57. [PubMed: 28301772]

(42). Frassek M; Arjun A; Bolhuis PG An Extended Autoencoder Model for Reaction Coordinate Discovery in Rare Event Molecular Dynamics Datasets. J. Chem. Phys 2021, 155, 064103. [PubMed: 34391359]

(43). Li Q; Lin B; Ren W Computing Committor Functions For the Study of Rare Events Using Deep Learning. J. Chem. Phys 2019, 151, 054112.

(44). Roux B Transition Rate Theory, Spectral Analysis, and Reactive Paths. J. Chem. Phys 2022, 156, 134111. [PubMed: 35395906]

(45). He Z; Chipot C; Roux B Committor-Consistent Variational String Method. J. Phys. Chem. Letters 2022, 13, 9263–9271.

(46). Krivov SV Blind Analysis of Molecular Dynamics. J. Chem. Theory Comput 2021, 17, 2725–2736. [PubMed: 33914517]

(47). Krivov SV Nonparametric Analysis of Nonequilibrium Simulations. J. Chem. Theory Comput 2021, 17, 5466–5481. [PubMed: 34464134]

(48). Noé F; Nüske F A Variational Approach to Modeling Slow Processes in Stochastic Dynamical Systems. Multiscale Model. Simul 2013, 11, 635–655.

(49). Merzbacher E Quantum Mechanics, 3rd Ed.; John Wiley & Sons, Inc.: New York, New York, 1998.

(50). Karlin S; Taylor HM A first course in stochastic processes, 2nd Edition; Academic Press Inc.: New York, NY, 1975.

(51). Nüske F; Keller BG; Pérez-Hernández G; Mey ASJS; Noé F Variational Approach to Molecular Kinetics. J. Chem. Theory Comput 2014, 10, 1739–1752. [PubMed: 26580382]

(52). Berezhkovskii A; Szabo A Ensemble of Transition States for Two-state Protein Folding from the Eigenvectors of Rate Matrices. J. Chem. Phys 2004, 121, 9186–9187. [PubMed: 15527389]

(53). Following Berezhkovskii and Szabo,[52] we first define a symmetric operator $S_\tau(\mathbf{z}' \mid \mathbf{z}) = S_\tau(\mathbf{z} \mid \mathbf{z}') = (\rho_{\mathrm{eq}}(\mathbf{z}'))^{-1/2}\mathscr{P}_\tau(\mathbf{z}' \mid \mathbf{z})(\rho_{\mathrm{eq}}(\mathbf{z}))^{1/2}$, using detailed balance. The left- and right-eigenvectors $\phi_k(\mathbf{z})$ of this symmetric operator are the same, with, $\psi_k^{\mathrm{R}}(\mathbf{z}) = (\rho_{\mathrm{eq}}(\mathbf{z}))^{1/2}\phi_k(\mathbf{z})$, and $\psi_k^{\mathrm{L}}(\mathbf{z}) = (\rho_{\mathrm{eq}}(\mathbf{z}))^{-1/2}\phi_k(\mathbf{z})$. Therefore, $\psi_k^{\mathrm{R}}(\mathbf{z}) = \rho_{\mathrm{eq}}(\mathbf{z})\psi_k^{\mathrm{L}}(\mathbf{z})$. Additional detail is available in the Supporting Information..

(54). Mitsutake A; Iijima H; Takano H Relaxation Mode Analysis of a Peptide System: Comparison with Principal Component Analysis. J. Chem. Phys 2011, 135, 164102. [PubMed: 22047223]

(55). Schwantes CR; Pande VS Improvements in Markov State Model Construction Reveal Many Non-native Interactions in the Folding of NTL9. J. Chem. Theory Comput 2013, 9, 2000–2009. [PubMed: 23750122]

(56). Pérez-Hernández G; Paul F; Giorgino T; De Fabritiis G; Noé F Identification of Slow Molecular Order Parameters for Markov Model Construction. J. Chem. Phys 2013, 139, 015102. [PubMed: 23822324]

(57). Bromley J; Bentz JW; Bottou L; Guyon I; Lecun Y; Moore C; Säckinger E; Shah R Signature Verification Using a “Siamese” Time Delay Neural Network. Int. J. Pattern Recognit. Artif. Intell 1993, 07, 669–688.

(58). Chicco D In Artificial Neural Networks; Cartwright H, Ed.; Methods in Molecular Biology; Springer US: New York, NY, 2021; pp 73–94.

(59). Noé F; Clementi C Kinetic Distance and Kinetic Maps from Molecular Dynamics Simulation. J. Chem. Theory. Comput 2015, 11, 5002–5011. [PubMed: 26574285]

(60). Bicout DJ; Szabo A Electron Transfer Reaction Dynamics in non-Debye Solvents. J. Chem. Phys 1998, 109, 2325–2338.

(61). Schumaker M; Pomes R; Roux B Framework Model for Single Proton Conduction through Gramicidin. Biophys. J 2001, 80, 12–30. [PubMed: 11159380]

(62). Rydzewski J; Valsson O Multiscale Reweighted Stochastic Embedding: Deep Learning of Collective Variables for Enhanced Sampling. J. Phys. Chem. A 2021, 125, 6286–6302. [PubMed: 34213915]

(63). Rosta E; Hummer G Free Energies from Dynamic Weighted Histogram Analysis Using Unbiased Markov State Model. J. Chem. Theory. Comput 2015, 11, 276–285. [PubMed: 26574225]

(64). E W; Ren W; Vanden-Eijnden E String Method for the Study of Rare Events. Phys. Rev. B 2002, 66, 052301.

(65). E W; Ren WQ; Vanden-Eijnden E Transition Pathways in Complex Systems: Reaction Coordinates, Isocommittor Surfaces, and Transition Tubes. Chem. Phys. Lett 2005, 413, 242–247.

(66). E W; Ren W; Vanden-Eijnden E Simplified and Improved String Method for Computing the Minimum Energy Paths in Barrier-crossing Events. J. Chem. Phys 2007, 126, 164103. [PubMed: 17477585]

(67). Maragliano L; Fischer A; Vanden-Eijnden E; Ciccotti G String Method in Collective Variables: Minimum Free Energy Paths and Isocommittor Surfaces. J. Chem. Phys 2006, 125, 24106. [PubMed: 16848576]

(68). E W; Ren W; Vanden-Eijnden E Finite Temperature String Method for the Study of Rare Events. J. Phys. Chem. B 2005, 109, 6688–6693. [PubMed: 16851751]

(69). Pan A; Sezer D; Roux B Finding Transition Pathways Using the String Method with Swarms of Trajectories. J. Phys. Chem. B 2008, 112, 3432–3440. [PubMed: 18290641]

(70). Branduardi D; Gervasio FL; Parrinello M From A to B in Free Energy Space. J. Chem. Phys 2007, 126, 054103. [PubMed: 17302470]

(71). Darve E; Pohorille A Calculating Free Energies Using Average Force. J. Chem. Phys 2001, 115, 9169–9183.

(72). Comer J; Gumbart JC; Hénin J; Lelièvre T; Pohorille A; Chipot C The Adaptive Biasing Force Method: Everything You Always Wanted To Know but Were Afraid To Ask. J. Phys. Chem. B 2015, 119, 1129–1151. [PubMed: 25247823]

(73). Díaz Leines G; Ensing B Path Finding on High-Dimensional Free Energy Landscapes. Phys. Rev. Lett 2012, 109, 020601. [PubMed: 23030145]

(74). Hovan L; Comitani F; Gervasio FL Defining an Optimal Metric for the Path Collective Variables. J. Chem. Theory Comput 2019, 15, 25–32. [PubMed: 30468578]

(75). Zhao T; Fu H; Lelièvre T; Shao X; Chipot C; Cai W The Extended Generalized Adaptive Biasing Force Algorithm for Multidimensional Free-Energy Calculations. J. Chem. Theory Comput 2017, 13, 1566–1576. [PubMed: 28253446]

(76). Fu H; Shao X; Cai W; Chipot C Taming Rugged Free Energy Landscapes Using an Average Force. Acc. Chem. Res 2019, 52, 3254–3264. [PubMed: 31680510]

(77). Clevert D-A; Unterthiner T; Hochreiter S Fast and Accurate Deep Network Learning by Exponential Linear Units (ELUs). 4th International Conference on Learning Representations, ICLR 2016, San Juan, Puerto Rico, May 2–4, 2016, Conference Track Proceedings. 2016.

(78). Kingma DP; Ba J Adam: A Method for Stochastic Optimization. 3rd International Conference on Learning Representations, ICLR 2015, San Diego, CA, USA, May 7–9, 2015, Conference Track Proceedings. 2015.

(79). Müller K; Brown LD Location of Saddle Points and Minimum Energy Paths by a Constrained Simplex Optimization Procedure. Theor. Chim. Acta 1979, 53, 75–93.

(80). Berezhkovskii A; Szabo A One-dimensional Reaction Coordinates for Diffusive Activated Rate Processes in Many Dimensions. J. Chem. Phys 2005, 122, 14503. [PubMed: 15638670]

(81). Phillips JC; Hardy DJ; Maia JDC; Stone JE; Ribeiro JV; Bernardi RC; Buch R; Fiorin G; Hénin J; Jiang W; McGreevy R; Melo MCR; Radak BK; Skeel RD; Singharoy A; Wang Y; Roux B; Aksimentiev A; Luthey-Schulten Z; Kalé LV; Schulten K; Chipot C; Tajkhorshid E Scalable molecular dynamics on CPU and GPU architectures with NAMD. J. Chem. Phys 2020, 153, 044130. [PubMed: 32752662]

(82). Fiorin G; Klein ML; Hénin J Using Collective Variables to Drive Molecular Dynamics Simulations. Mol. Phys 2013, 111, 3345–3362.

(83). Fu H; Chen H; Wang X; Chai H; Shao X; Cai W; Chipot C Finding an Optimal Pathway on a Multidimensional Free-Energy Landscape. J. Chem. Inf. Model 2020, 60, 5366–5374. [PubMed: 32402199]

(84). MacKerell AJ; Bashford D; Bellot M; Dunbrack R; Evanseck J; Field M; Fischer S; Gao J; Guo H; Ha S, D. J-M; Kuchnir L; Kuczera K; Lau F; Mattos C; Michnick S; Ngo T; Nguyen D; Prodhom B; Reiher III W; Roux B; Schlenkrich M; Smith J; Stote R; Straub J; Watanabe M; Wiorkiewicz-Kuczera J; Karplus M All-atom Empirical Potential for Molecular Modeling and Dynamics Studies of Proteins. J. Phys. Chem. B 1998, 102, 3586–3616. [PubMed: 24889800]

(85). Bonfanti S; Kob W Methods to Locate Saddle Points in Complex Landscapes. J. Chem. Phys 2017, 147, 204104. [PubMed: 29195295]

(86). Sun L; Vandermause J; Batzner S; Xie Y; Clark D; Chen W; Kozinsky B Multitask Machine Learning of Collective Variables for Enhanced Sampling of Rare Events. J. Chem. Theory Comput 2022, 18, 2341–2353. [PubMed: 35274958]

(87). Vlachas PR; Zavadlav J; Praprotnik M; Koumoutsakos P Accelerated Simulations of Molecular Systems through Learning of Effective Dynamics. J. Chem. Theory Comput 2022, 18, 538–549. [PubMed: 34890204]

(88). Tiwary P; Parrinello M From Metadynamics to Dynamics. Phys. Rev. Lett 2013, 111, 230602. [PubMed: 24476246]

(89). Rosso L; Abrams JB; Tuckerman ME Mapping the Backbone Dihedral Free-Energy Surfaces in Small Peptides in Solution Using Adiabatic Free-Energy Dynamics. J. Phys. Chem. B 2005, 109, 4162–4167. [PubMed: 16851477]

(90). Trstanova Z; Leimkuhler B; Lelièvre T Local and Global Perspectives on Diffusion Maps in the Analysis of Molecular Systems. Proc. Math. Phys. Eng. Sci 2020, 476, 20190036. [PubMed: 32082050]

(91). Donati L; Hartmann C; Keller BG Girsanov Reweighting for Path Ensembles and Markov State Models. J. Chem. Phys 2017, 146, 244112. [PubMed: 28668056]

(92). Kieninger S; Donati L; Keller BG Dynamical Reweighting Methods for Markov Models. Curr. Opin. Struct. Biol 2020, 61, 124–131. [PubMed: 31958761]

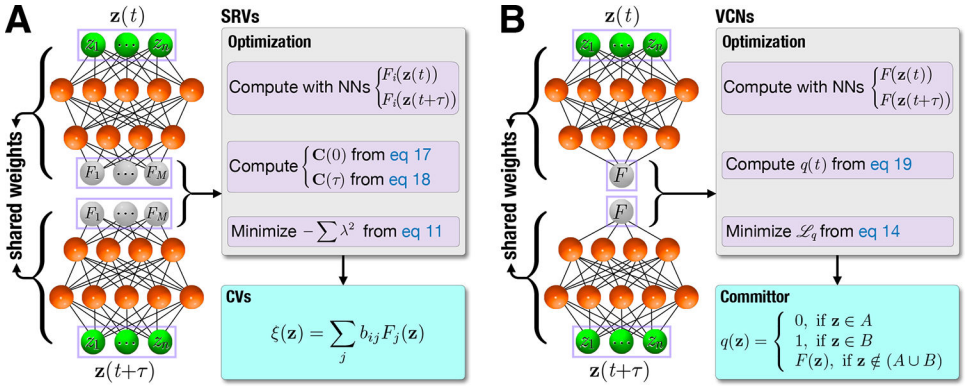

Figure 1:

Schematic representations of the Siamese neural networks used for the discovery of the slowest decorrelating collective variable (A) and of the committor probability (B). Computation of the loss functions is described on the right-hand side of panels A and B. For the state-free reversible variational approach for Markov processes networks (VAMPnets), or SRVs (A), the dimension of the latent space is $n \ll N$. For the variational committor-based neural networks (VCNs) (B), the dimension of the latent space is one.

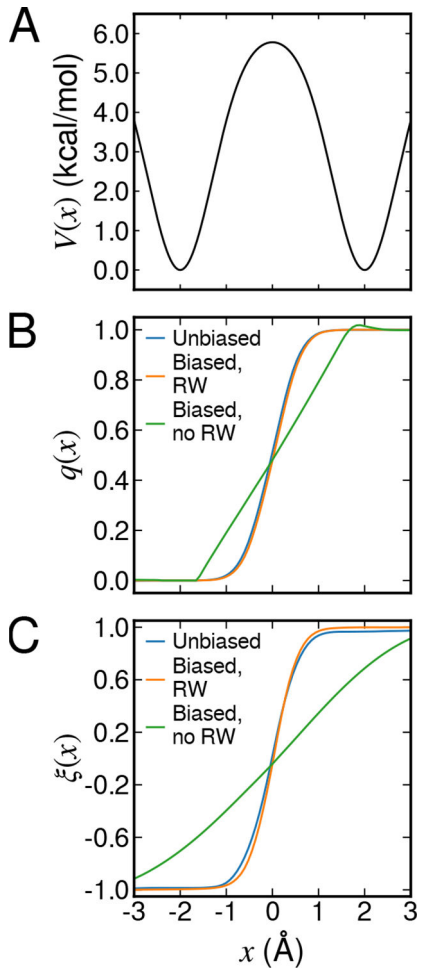

Figure 2:

(A) One-dimensional double-well potential $V(x)$. (B) Learned committor functions along x from an unbiased trajectory (blue), a WTM-eABF biased trajectory with reweighting in eq 22 (orange), and the same biased trajectory but without reweighting (green). (C) Learned CVs from SRVs along x from an unbiased trajectory (blue), a WTM-eABF biased trajectory with reweighting in eq 22 (orange), and the same biased trajectory but without reweighting (green).

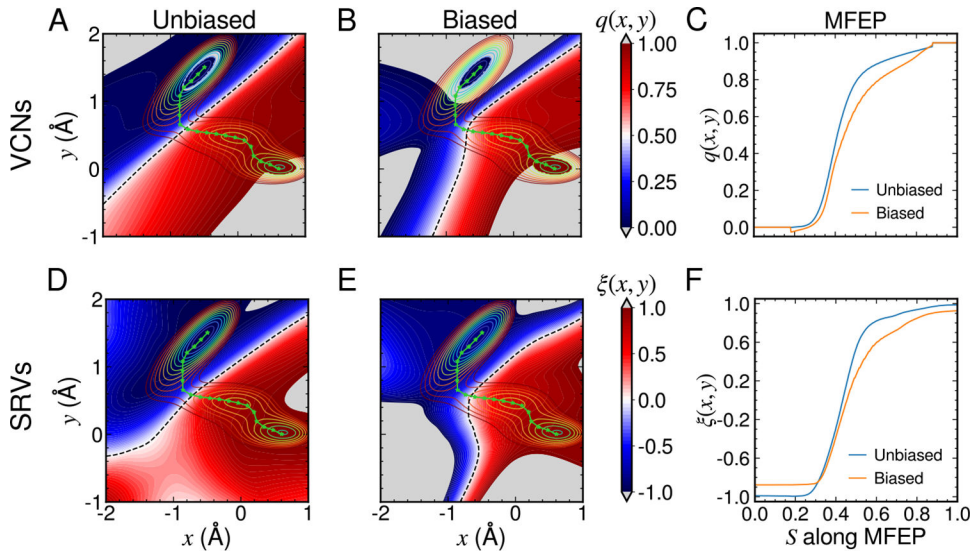

Figure 3:

The learned committor functions $q(x, y)$ for the Müller-Brown potential projected on (x, y) from an unbiased trajectory (A) and a biased trajectory along the path collective variable s (B). The learned CVs $\xi(x, y)$ by SRVs of the Müller-Brown potential projected on (x, y) from an unbiased trajectory (D) and a biased trajectory along the path collective variable s (E). $q(x, y)$ and $\xi(x, y)$ along the MFEP (green lines) are shown in (C) and (F), respectively. The contour lines in (A), (B), (D) and (E) in rainbow colors depict the potential energy surface. The dashed lines in (A) and (B) highlight the isosurface of $q(x, y) = 0.5$. The dashed lines in (D) and (E) highlight the isosurface of $\xi(x, y) = 0$.

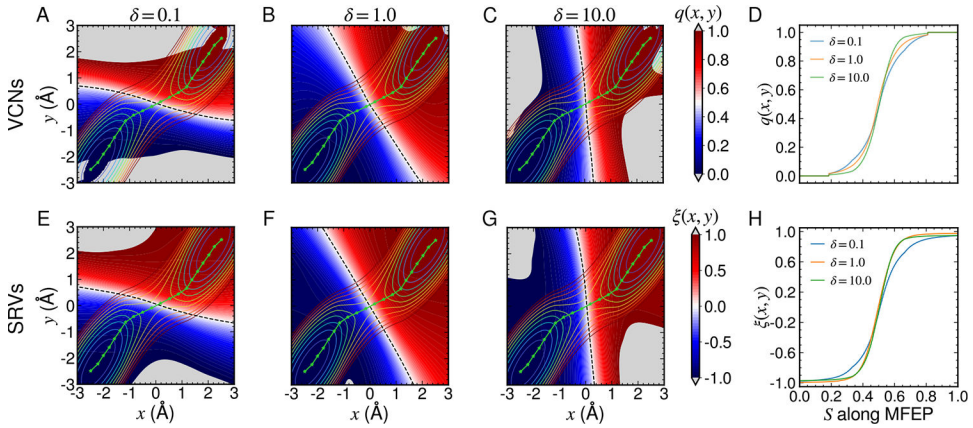

Figure 4:

The learned committor functions $q(x, y)$ projected on (x, y) for the Berezhkovskii-Szabo potential from unbiased trajectories with $\delta = 0.1$ (A), $\delta = 1.0$ (B) and $\delta = 10.0$ (C). The learned CVs $\xi(x, y)$ projected on (x, y) from unbiased trajectories with $\delta = 0.1$ (E), $\delta = 1.0$ (F) and $\delta = 10.0$ (G). The $q(x, y)$ and $\xi(x, y)$ from unbiased simulations along the MFEP (green lines) in different δs are shown in (D) and (E), respectively. The contour lines in (A-C) and (E-G) in rainbow colors depict the potential energy surface. The dashed lines in (A-C) highlight the isosurface of $q(x, y) = 0.5$. The dashed lines in (E-G) highlight the isosurface of $\xi(x, y) = 0$.

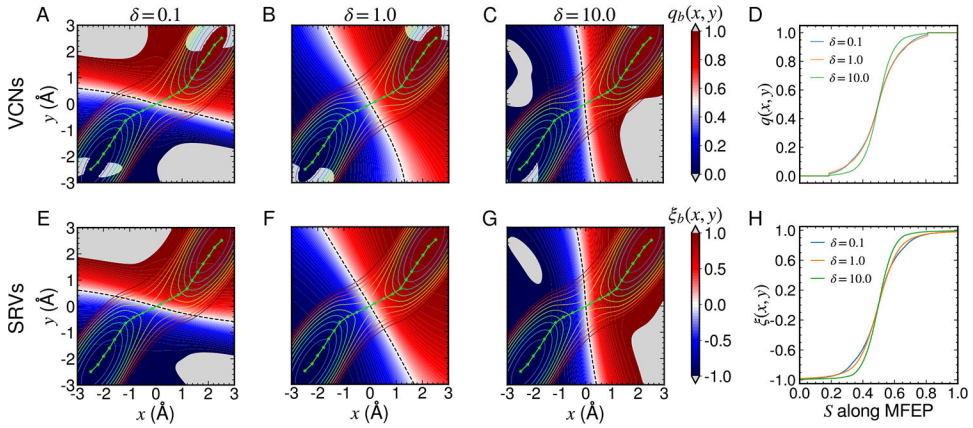

Figure 5:

The learned committor functions $q(x, y)$ projected on (x, y) for the Berezhkovskii-Szabo potential from WTM-eABF biased simulations along the PCV s with $\delta = 0.1$ (A), $\delta = 1.0$ (B) and $\delta = 10.0$ (C). The learned CVs $\xi(x, y)$ projected on (x, y) from WTM-eABF biased simulations along the PCV s with $\delta = 0.1$ (E), $\delta = 1.0$ (F) and $\delta = 10.0$ (G). The $q(x, y)$ and $\xi(x, y)$ from the biased simulations along the MFEP (green lines) in different δs are shown in (D) and (E), respectively. The contour lines in (A-C) and (E-G) in rainbow colors depict the potential energy surface. The dashed lines in (A-C) highlight the isosurface of $q(x, y) = 0.5$. The dashed lines in (E-G) highlight the isosurface of $\xi(x, y) = 0$.

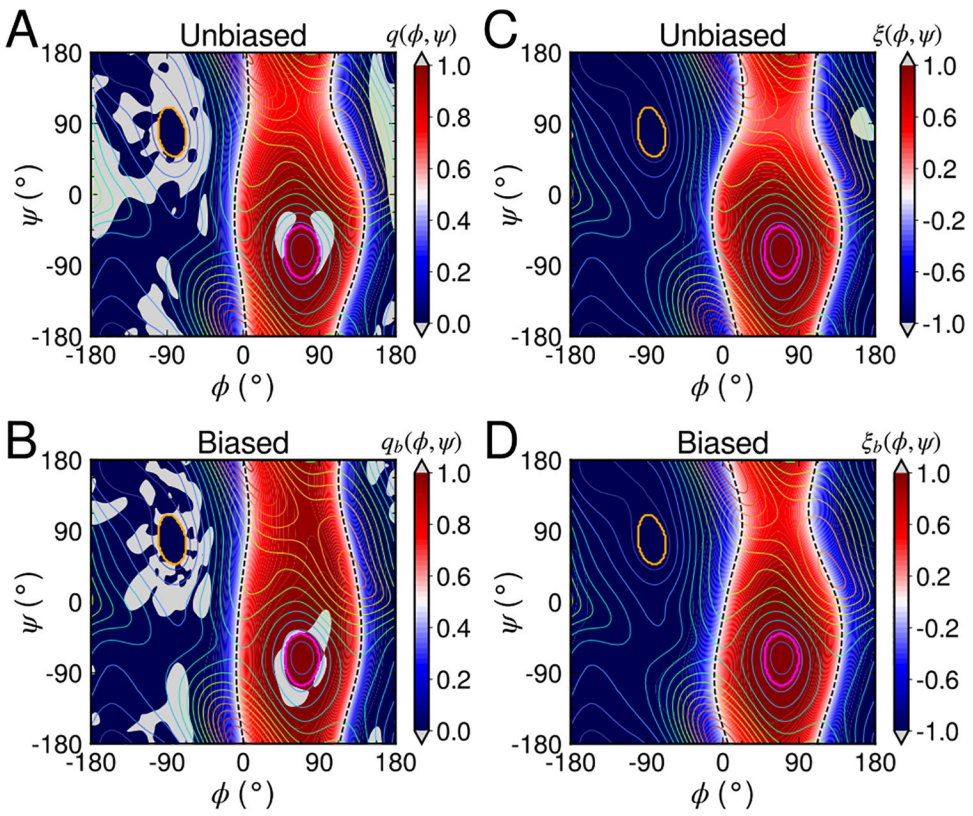

Figure 6:

The learned committor projected on ϕ and ψ for the isomerization of N-acetyl-N′-methylalanylamide from (A) an unbiased trajectory and (B) a biased trajectory of the WTM-eABF simulation along ϕ and ψ. The learned CV projected onto ϕ and ψ for the same biological process from (C) an unbiased trajectory and (D) a WTM-eABF biased trajectory along ϕ and ψ. The contour lines in rainbow colors depict the free-energy landscape along ϕ and ψ. The two metastable states, C_{7eq} and C_{7ax}, are highlighted with the orange and purple ellipses, respectively.

Table 1:

Summary of the transition rates k_{AB}

Potential	Transition rate $k_{AB}\left(\mathrm{ps}^{-1}\right)$				
	MFPT	SRVs		VCNs	
	Unbiased	Unbiased	Biased	Unbiased	Biased
Double-well 1D	4.93×10^{-4}	4.37×10^{-4}	4.16×10^{-4}	4.07×10^{-4}	4.26×10^{-4}
2D MB[1]	5.37×10^{-4}	5.45×10^{-4}	5.76×10^{-4}	4.97×10^{-4}	6.12×10^{-4}
2DBS[2]$(\gamma_x/\gamma_y = 0.1)$	3.37×10^{-3}	3.72×10^{-3}	3.19×10^{-3}	3.70×10^{-3}	3.08×10^{-3}
2D BS[2]$(\gamma_x/\gamma_y = 1.0)$	1.07×10^{-2}	1.18×10^{-2}	1.95×10^{-2}	1.02×10^{-2}	1.76×10^{-2}
2D BS[2]$(\gamma_x/\gamma_y = 10.0)$	1.87×10^{-3}	1.90×10^{-3}	1.52×10^{-3}	1.99×10^{-3}	1.50×10^{-3}
NANMA[3]	1.34×10^{-5}	1.71×10^{-5}	1.09×10^{-5}	1.24×10^{-5}	1.73×10^{-5}

[1]Two-dimensional Müller-Brown potential.

[2]Two-dimensional Berezhkovskii-Szabo potential.

[3]N-acetyl-N′-methylalanylamide (dialanine).